Evaluation of models for bubble-induced turbulence by DNS and utilization in two-fluid model computations of an industrial pilot-scale bubble column

Sercan Erdogan[a], Thomas Schulenberg[b], Olaf Deutschmann[a,c], Martin Wörner[a,*]

[a]*Karlsruhe Institute of Technology (KIT), Institute of Catalysis Research and Technology, Engesser Straße 20, 76131 Karlsruhe, Germany*
[b]*Karlsruhe Institute of Technology (KIT), Institute for Thermal Energy Technology and Safety, Hermann-von-Helmholtz-Platz 1, 76344 Eggenstein-Leopoldshafen, Germany*
[c]*Karlsruhe Institute of Technology (KIT), Institute for Chemical Technology and Polymer Chemistry, Engesser Straße 20, 76131 Karlsruhe, Germany*

Abstract

This paper presents numerical studies on modeling of bubble induced turbulence at two significantly different scales. On the scale of a bubble swarm, direct numerical simulations are performed with a geometric volume-of-fluid method and the budget equation of liquid phase turbulence kinetic energy is analyzed. By *a priori* testing of models for the interfacial term in this equation, suitable closure relations are identified. On the scale of an industrial bubble column, simulations with a two-fluid model are performed with water and cumene as liquid phases under elevated pressures. Turbulence is taken into account by a mixture $k - \varepsilon$ model, considering two closure relations for the interfacial term identified from the DNS. For both liquids, an influence of the model for the interfacial term on turbulence kinetic energy and gas holdup is found, which is, however, small at elevated pressures. Numerical results for local and overall gas holdup are in reasonable agreement with measurements reported for this industrial pilot-scale bubble column. For the overall gas holdup, an empirical correlation from literature is identified which predicts the present numerical results reasonably well.

Keywords: Direct Numerical Simulation, Bubbly flow, Budget of

*Corresponding author, Email: martin.woerner@kit.edu (M. Wörner)

1. Introduction

Bubble columns (BC) are widely used as multiphase reactors in chemical, biochemical and petrochemical industries [1, 2]. Depending on conditions, they operate either in a bubbly flow (homogeneous) regime or churn-turbulent flow (heterogeneous) regime [3]. Industrial production in bubble columns is usually conducted at above atmospheric pressures and above ambient temperatures in processes primarily involving the use of organic liquids [4]. Despite this fact, common academic research has been focused on the description of bubble column hydrodynamics under atmospheric conditions most often in aqueous systems. Furthermore, many experiments consider lab scale bubble columns while studies in pilot-plant scale such as in [5–7] are still relatively rare.

The design of industrial scale bubble columns is currently based on experience, empirical correlations, one-dimensional convection-dispersion models and compartment models. Such approaches remain certainly limited when an increase in reactor performance is sought. Multidimensional Computational Fluid Dynamics (CFD) methods based on the Reynolds-averaged Navier-Stokes (RANS) equations are potentially attractive for this purpose [8–12]; however, their use is nowadays often limited to lab-scale bubble columns and aqueous liquids, and not yet used as a tool for design of industrial scale bubble columns. One shortcoming of RANS-based CFD methods such as the widely used Euler-Euler (EE) approach (two-fluid model) is the lack of proper models for bubble-induced turbulence (BIT) [13]. Velocity fluctuations in BIT show statistical features (such as spectra [14] and probability density functions [15, 16]) that notably differ from turbulence in liquid single-phase flows. In pressure-driven bubbly flows, turbulence is not the simple sum of BIT and single-phase flow turbulence. Instead bubbles may augment or suppress single-phase turbulence depending on conditions [17], with turbulence anisotropy depending on bubble Reynolds number [18].

While in practical engineering CFD applications with gas-liquid flows, the latter differences are often ignored by applying single-phase turbulence models, the efforts on the academic side to develop improved turbulence models specially suited for bubbly flows are increasing [18–24]. Particularly useful in this context in addition to experiments [25] are direct numerical simulations

2

(DNS) since these allow evaluating statistical flow features and quantities (e.g., containing pressure fluctuations) which can hardly be measured, especially for practically relevant void fractions [26–28]. The DNS data can be used to evaluate budgets of turbulent kinetic energy and for *a priori* testing of models proposed for various closure terms. While the latter approach has long been well established e.g. for opaque single-phase flows [29, 30], this is not the case for two-phase flows. For bubbly flows, it has first been applied by Ilic [31–33] for purely buoyancy-driven flow and is becoming increasingly popular now for pressure-driven bubbly flows [20, 34–36].

This contribution focuses on the testing of statistical models for bubble-induced turbulence in the homogeneous regime at various scales. For this purpose, an integrated computational methodology is adopted. It covers swarms of millimeter-sized bubbles computed by DNS as well as an industrial pilot-scale bubble column computed by the EE method. In the latter approach, both aqueous and organic systems under atmospheric and elevated pressure are investigated and numerical results are compared with measurements reported in literature [6, 37].

The outline of the paper is as follows. Section 2 introduces the DNS of bubble swarms. The DNS results are used in Section 3 to study the budget of liquid phase turbulence kinetic energy and to test closure relations for the interfacial term. Section 4 is devoted to the EE simulation of the pilot-scale bubble column.

2. Direct numerical simulations of bubbles rising in liquid

This section provides a compact overview of the direct numerical simulations performed in this study. After a brief description of the mathematical method, the computational setup is introduced. Suitable physical and numerical parameters for bubble swarm simulations are identified by preliminary simulations with single bubbles rising in stagnant liquid. On this basis, direct numerical simulations of monodisperse bubble swarms rising in a narrow gap between two vertical planes are performed for bubbles of different diameter.

2.1. Volume-of-fluid method

The direct numerical simulations are performed by the in-house computer code TURBIT-VOF which uses a geometric volume-of-fluid method with piecewise linear interface calculation (PLIC) in combination with unsplit advection for description of interface evolution. The code solves the lo-

3

cally volume-averaged two-phase Navier–Stokes equation assuming fully mobile interfaces (no contamination by surfactants) in non-dimensional single-field formulation for two incompressible Newtonian fluids on a regular staggered Cartesian mesh by a finite volume method. Time integration of the momentum equation is performed by an explicit third order Runge–Kutta method. For approximation of spatial derivatives, second order central difference schemes are used. A divergence free velocity field is ensured at the end of each time step by a projection method, where the pressure Poisson equation is solved by a conjugate gradient technique. For details on the governing equations, numerical aspects and code validation we refer to [38–42].

2.2. Simulation set-up in DNS

We consider a cubic computational domain with side length L_{ref}, aimed to mimic a sub-region of a flat bubble column (Fig. 1). In vertical (x) and span-wise (y) directions, periodic boundary conditions apply, whereas in z-direction the domain is bounded by two lateral vertical sidewalls with no-slip conditions. The lateral walls are essential to establish a direction along which statistical quantities are non-homogeneous (i.e., vary) so that gradient-dependent transport terms in the analytical budget-equation for turbulence kinetic energy do not vanish. The computational domain is discretized by a Cartesian grid which is uniform in the x- and y-directions (cell size h) but optionally non-uniform in z-direction. A volumetric force density is chosen so that the rising bubbles drive an upward liquid flow in the channel center, whereas near the lateral walls the liquid flows downward [43].

2.3. Preliminary investigations with single bubbles

To determine suitable physical and numerical parameters for bubble swarm simulations, comprehensive preliminary simulations with single bubbles rising in stagnant liquid have been performed for various values of Eötvös number $Eo = g(\rho_{\text{L}} - \rho_{\text{G}})d_{\text{B}}^2/\sigma$ and Morton number $M = g(\rho_{\text{L}} - \rho_{\text{G}})\mu_{\text{L}}^4/(\rho_{\text{L}}^2\sigma^3)$, where σ is the coefficient of surface tension and $g = 9.81$ m/s^2 the gravitational acceleration. The results revealed that a uniform grid corresponding to a resolution of 20 mesh cells per bubble diameter (d_{B}), a gas-to-liquid density ratio ($\rho_{\text{G}}/\rho_{\text{L}}$) of 1/25 and a gas-to-liquid viscosity ratio ($\mu_{\text{G}}/\mu_{\text{L}}$) below 1/2 are appropriate to obtain results that are independent from the mesh size, the gas density, and the gas viscosity [43]. The latter findings are in agreement with DNS results reported by Cano-Lozano et al. [45], stating that gas phase properties hardly affect the bubble terminal velocity and shape.
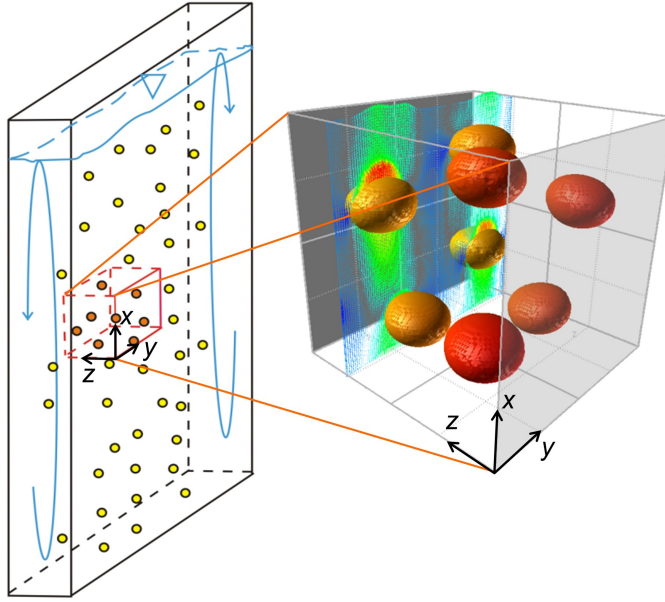
4

Figure 1: Sketch of a flat bubble column (left) with the subregion representing the computational domain and a DNS snapshot (right). (Color version of b/w figure from [44] reprinted with permission from Wiley.)

2.4. Bubble swarm simulations

The direct numerical simulations of bubble swarms aim to support the selection of adequate models for the interfacial term in the turbulence kinetic energy equation for EE computations of bubble column reactors operated at elevated pressure and temperature, especially for organic liquids such as cumene. Bothe et al. [7] give physical properties of cumene at temperatures of 35 and 70°C and pressures of 1 and 18.5 bar. For the present DNS study, liquid density and coefficient of surface tension are chosen similarly and set to $\rho_{\mathrm{L}} = 867$ kg/m^3 and $\sigma = 28$ mN/m, respectively. For reasons explained next, liquid viscosity is set to $\mu_{\mathrm{L}} = 5$ mPa s, a value that is about six times larger than the viscosity of cumene.

The increase in the liquid viscosity is related to the focus of the present study, which is on monodisperse flow. It turned out that for the Morton number of cumene, $M = 2.2 \times 10^{-10}$ [6], and for the relevant range of bubble diameters, $d_{\mathrm{B}} \approx 1 - 4$ mm [7], no monodisperse conditions could be preserved with the code. Instead, coalescence events between bubbles occurred frequently in the DNS at such low Morton numbers [43]. By increasing the

5

liquid viscosity, the Morton number is increased to $M = 3.1 \times 10^{-7}$. Under these conditions, physical and numerical coalescence (cf. [44, Fig. 2]) are largely avoided. Physical properties of the disperse phase correspond to $\mu_G/\mu_L = 1/3$ and $\rho_G/\rho_L = 1/25$. Simulations are started with both phases at rest and randomly distributed spherical bubbles.

Simulations are performed for three different values of the bubble diameter (1.6, 2 and 3 mm), resulting in values of the Eötvös number in the range $0.747 \leq Eo \leq 2.625$, see Table 1. For each bubble diameter, the computational domain is a cube with side length $L_{\text{ref}} = 5d_B$. Simulations are performed on a grid comprising $100 \times 100 \times 120$ mesh cells. In z-direction, the grid size smoothly changes from $0.5h$ at the wall to h in the channel center, where the grid is isotropic. The grid refinement close to the side walls serves to resolve the thin lateral liquid film that forms as bubbles approach the wall, to avoid artificial wall contact of bubbles in the simulations. The number of bubbles (N_B) in the simulations is either five or six, resulting in values of the overall gas holdup (ϵ_G) of 2.1% and 2.5%, respectively. The bubble shapes are unsteady but about ellipsoidal with typical aspect ratio (depending on Eo) in the range $0.7 - 0.85$, cf. the DNS snapshot in Fig. 1. For Case C in Table 1 with $\epsilon_G = 2.5\%$, two coalescence events occurred in the course of the simulation so that finally only four bubbles retained (two with original volume and two with double volume) and the flow is actually bidisperse. From the mean rise velocity of the bubbles in the swarm (U_{swarm}), a mean bubble Reynolds number $Re_{\text{swarm}} = \rho_L d_B U_{\text{swarm}}/\mu_L$ is computed. As shown in Table 1, Re_{swarm} increases with an increase of d_B and – for a fixed value of d_B – with an increase of ϵ_G. After bubbles have reached about their terminal velocity, a domain replication methodology in the two periodic directions is applied for cases without coalescence [43]. Thereby, N_B and the size of the computational domain are increased by a factor of four while the void fraction is preserved. The simulations in the enlarged domains are continued and statistically analyzed in Section 3. The present DNS study extends that of Ilic [31] to a larger number of bubbles in a wider range of Eo for lower values of M. It should be noted, however, that N_B is still quite small so that statistical quantities evaluated from the DNS data may actually be not independent on N_B.

The last line in Table 1 shows the ratio between grid size (h) and Kolmogorov length scale $\eta_K = (\nu_L^3/\varepsilon_L^{\text{av}})^{1/4}$ for each case, where $\nu_L = \mu_L/\rho_L$ and $\varepsilon_L^{\text{av}}$ is the averaged dissipation (computed as integral of the local dissipation profile, cf. Sect. 3). As the ratio h/η_K is about 1 or below, the pseudo-

6

turbulence can be considered to be adequately resolved by the grid.

Table 1: Parameters in DNS cases A–D ($M = 3 \times 10^{-7}$).

Parameter	Unit	Case A	Case B	Case C	Case D
d_B	mm	1.6	2.0	2.0	3.0
Eo	–	0.747	1.167	1.167	2.625
N_B	–	5	5	6 (4)	5
ϵ_G	%	2.1	2.1	2.5	2.1
Re_swarm	–	35	55	60	115
h/η_K	–	0.48	0.65	0.69	1.10

3. Analysis of liquid phase turbulence kinetic energy

In this section, the DNS data are used to analyze the liquid phase turbulence kinetic energy (k_L), as well as the budget of the analytical transport equation for k_L. The closed form of this equation is a cornerstone of many statistical turbulence models. Besides, DNS data are used to *a priori* test closure assumptions for the interfacial term in the modeled k_L-equation.

3.1. Statistical evaluation of DNS data

The analysis of the liquid phase turbulence kinetic energy and its transport equation requires appropriate averaging of the instantaneous DNS flow field. For the bubbly flow between vertical parallel plates, the vertical and span-wise directions can be considered as homogeneous, which allows the spatial averaging over vertical slabs of mesh cells parallel to the channel walls. This averaging procedure (see [31, 33] for details) yields profiles of statistical quantities, which depend on the wall-normal coordinate z. The plane averaging is performed for a certain number of instants in time when the DNS has reached about a statistically stationary state. The profiles obtained for different instants within a certain time interval are then linearly averaged. The respective plane and time averaging is denoted by a double over-bar while deviations from this mean are denoted by prime symbol. With this notation, the liquid phase turbulence kinetic energy is given by

$$k_\mathrm{L} = \frac{1}{2}\overline{\overline{\mathbf{u}'_\mathrm{L} \cdot \mathbf{u}'_\mathrm{L}}}. \tag{1}$$
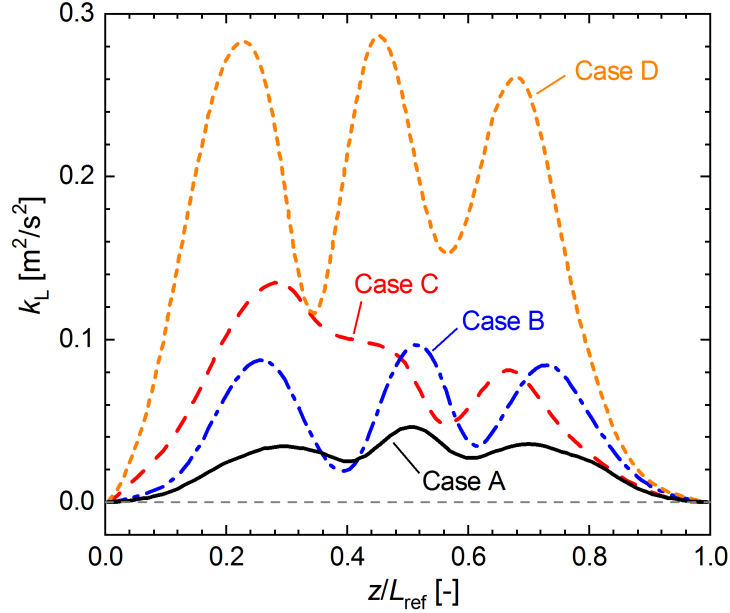
7

Figure 2: Wall-normal profiles of k_L for DNS cases A–D in Table 1.

3.2. Spatial distribution of liquid phase turbulence kinetic energy

In Fig. 2, the wall-normal profiles of k_L are plotted for the four cases in Table 1. It can be seen that the local maximum and the integral of k_L increase with an increase of d_B, Eo and Re_swarm. For Cases A, B and D, the profiles of k_L are almost symmetrical with respect to the channel mid-plane as they should be. For Case C, where coalescence occurred, the flow is bidisperse in the time interval of the statistical analysis. Therefore, the profile of k_L is not symmetrical and exhibits larger values in the left half of the channel where the two larger bubbles rise and void fraction is higher. Case C is not considered further.

3.3. Budget of analytical transport equation for k_L

According to Kataoka and Serizawa [46], the averaged transport equation for liquid phase turbulence kinetic energy in incompressible gas-liquid two-phase flow without phase change is given by the following analytical (i.e., unclosed) form

$$\frac{\partial}{\partial t}(\alpha_\mathrm{L} k_\mathrm{L}) + \nabla \cdot (\alpha_\mathrm{L} k_\mathrm{L} \overline{\overline{\mathbf{u}_\mathrm{L}}}) = P_\mathrm{L}^\mathrm{an} + D_\mathrm{L}^\mathrm{an} + \varepsilon_\mathrm{L}^\mathrm{an} + S_\mathrm{L}^\mathrm{an}. \qquad (2)$$

8

Here, $\alpha_{\mathrm{L}} = 1 - \alpha_{\mathrm{G}}$ is the liquid volume fraction and $\overline{\overline{\mathbf{u}_{\mathrm{L}}}}$ is the averaged velocity. The production term due to shear ($P_{\mathrm{L}}^{\mathrm{an}}$), the diffusion term ($D_{\mathrm{L}}^{\mathrm{an}}$) and the dissipation ($\varepsilon_{\mathrm{L}}^{\mathrm{an}}$) are given by

$$P_{\mathrm{L}}^{\mathrm{an}} = -\alpha_{\mathrm{L}} \overline{\overline{\mathbf{u}_{\mathrm{L}}' \mathbf{u}_{\mathrm{L}}'}} : \nabla \overline{\overline{\mathbf{u}_{\mathrm{L}}}}, \tag{3}$$

$$D_{\mathrm{L}}^{\mathrm{an}} = \nabla \cdot \left(\rho_{\mathrm{L}}^{-1} \alpha_{\mathrm{L}} \overline{\overline{\tau_{\mathrm{L}}' \cdot \mathbf{u}_{\mathrm{L}}'}} \right) - \nabla \cdot \left(\rho_{\mathrm{L}}^{-1} \alpha_{\mathrm{L}} \overline{\overline{p_{\mathrm{L}}' \mathbf{u}_{\mathrm{L}}'}} + 0.5 \alpha_{\mathrm{L}} \overline{\overline{(\mathbf{u}_{\mathrm{L}}' \cdot \mathbf{u}_{\mathrm{L}}') \mathbf{u}_{\mathrm{L}}'}} \right), \tag{4}$$

$$\varepsilon_{\mathrm{L}}^{\mathrm{an}} = -\rho_{\mathrm{L}}^{-1} \alpha_{\mathrm{L}} \overline{\overline{\tau_{\mathrm{L}}' : \nabla \mathbf{u}_{\mathrm{L}}'}}, \tag{5}$$

where τ_{L}' is the fluctuating viscous stress tensor [46]. The latter three terms are analogous to the single-phase turbulence kinetic energy equation with α_{L} as a prefactor. The interfacial term in Eq. (2) is given by

$$S_{\mathrm{L}}^{\mathrm{an}} = \overline{\rho_{\mathrm{L}}^{-1} (\tau_{\mathrm{L,int}}' - p_{\mathrm{L,int}}' \mathbb{I}) \cdot \mathbf{u}_{\mathrm{L,int}}' \cdot \mathbf{n}_{\mathrm{L}} a_{\mathrm{int}}} \tag{6}$$

and represents an additional source term, which is absent in single-phase flow. Here, the index $(.)_{\mathrm{L,int}}$ indicates that the respective quantity is evaluated at the liquid side of the phase boundary, $\mathbf{n}_{\mathrm{L}}$ is the unit normal vector at the interface directed towards the gas phase and a_{int} is the interfacial area concentration (which is evaluated here from the PLIC surfaces).

Fig. 3 shows the budgets of k_{L} for Cases A, B and D where no coalescence occurs together with the local gas content (α_{G}). The profiles for α_{G} and the four terms on the right-hand-side of Eq. (2) are evaluated from the DNS data using the averaging procedure described in Section 3.1. The terms on the left-hand-side of Eq. (2) are not evaluated individually; instead they are represented together by the out-of-balance term resulting from summing up the four terms on the right-hand-side of Eq. (2). The finite values of the out-of-balance term suggest that no statistically fully quasi-steady states have been reached in the DNS. Furthermore, the profiles of α_{G} (and those of k_{L} in Fig. 2) are not flat in the channel center as one would expect for the homogeneous flow regime, owing to the rather smaller wall distance of only $5 d_{\mathrm{B}}$.

Despite the latter limitations, some clear findings can be reported from Fig. 3. For all cases, the main source term for the turbulence kinetic energy is due to interfacial effects ($S_{\mathrm{L}}^{\mathrm{an}}$), while the production by shear stresses ($P_{\mathrm{L}}^{\mathrm{an}}$) is negligible for the conditions examined in this work. The profiles of the interfacial term $S_{\mathrm{L}}^{\mathrm{an}}$ closely follow the profiles of the local gas content, which is reasonable. While for all cases the overall gas content is $\epsilon_{\mathrm{G}} =$

9

2.1%, the local gas content α_G takes maximum values up to $5 - 6\%$. The dissipation term ε_L^{an} is not in local equilibrium with the interfacial source term S_L^{an}. Instead, the excess of production of k_L in regions with high local gas content is redistributed by diffusion D_L^{an} into regions with low gas content (especially towards the walls). . The comparison of Fig. 3 (a)–(c) shows that the magnitudes of the interfacial term and the dissipation both increase with increase of d_B and Re_{swarm}. The reported findings show that for a reliable calculation of flows in bubble columns with the EE RANS approach, an adequate modeling of the interfacial term in the k_L-equation is of great importance.

3.4. A priori testing of models for the interfacial term

The wall-normal profiles of the interfacial term S_L^{an} in the analytical k_L-equation obtained from the DNS data are now compared with predictions for this term by different models. This so-called *a priori* testing allows identifying promising model approaches as well as model deficiencies. Several modeling approaches have been proposed for closure of this term, see e.g. [47].

In this paper, four different models for S_L^{an} are considered, namely the models proposed by Ishii and Mishima (IM) [48], Pfleger and Becker (PB) [49], Olmos, Gentric, and Midoux (OGM) [50] and Lahey [51]. As shown in Table 2, all these models relate S_L^{an} in different but linear manner to the work W_D of the drag force $\mathbf{F}_D$ given by

$$W_D = \underbrace{F_D}_{=|\mathbf{F}_D|} \underbrace{|\overline{\overline{\mathbf{u}_G}} - \overline{\overline{\mathbf{u}_L}}|}_{=u_{rel}} = \frac{3}{4} C_D \frac{\alpha_G \rho_L}{d_B} |\overline{\overline{\mathbf{u}_G}} - \overline{\overline{\mathbf{u}_L}}|^3. \tag{7}$$

While different relations for the drag coefficient C_D are used in [48–51], here one unique relation is considered to allow for a better comparison. For this purpose, the correlation

$$C_D^{To} = \max \left\{ \min \left[\frac{16}{Re_B}(1 + 0.15 Re_B^{0.687}), \frac{48}{Re_B} \right], \frac{8}{3} \frac{Eo}{Eo + 4} \right\} \tag{8}$$

proposed by Tomiyama et al. [52] for pure systems is used, where $Re_B = \rho_L d_B u_{rel}/\mu_L$. Interestingly, for different DNS cases, different sub-models in Eq. (8) become relevant and the active sub-model for a given case may even change with wall distance [43, Fig. 33].

Fig. 4 shows the wall normal profiles of S_L^{an} and the gas content as evaluated by the averaging procedure described in Section 3.1 for the DNS Cases
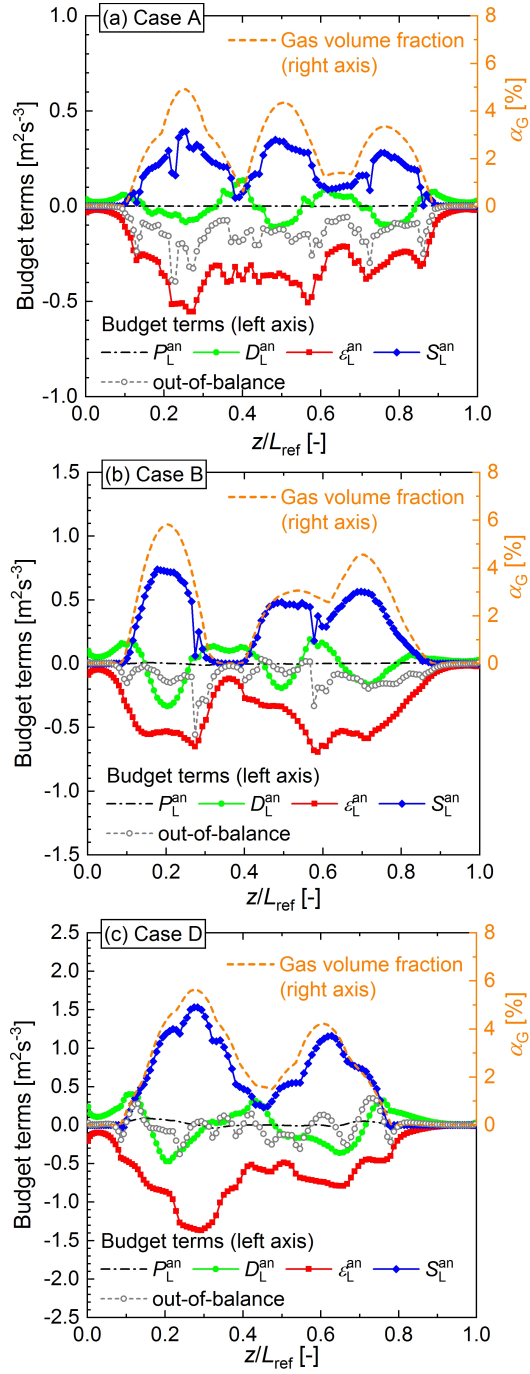
10

Figure 3: Budgets of analytical k_L-equation evaluated from DNS data: (a) Case A, (b) Case B, (c) Case D.

11

Table 2: Models (S_L^md) for the analytical interfacial term (S_L^an) in the k_L-equation.

Reference	S_L^md	Model formulation
Ishii and Mishima [48]	S_L^IM	W_D
Pfleger and Becker [49]	S_L^PB	$1.44\alpha_\mathrm{L}W_\mathrm{D}$
Olmos, Gentric, and Midoux [50]	$S_\mathrm{L}^\mathrm{OGM}$	$0.75W_\mathrm{D}$
Lahey [51]	$S_\mathrm{L}^\mathrm{Lahey}$	$[(1 + C_\mathrm{D}^{3/4})/(3C_\mathrm{D})]W_\mathrm{D}$

A, B and D. In addition, profiles for the four models for S_L^an listed in Table 2 are displayed. To this end, first the right-hand-side of Eq. (7) is evaluated from the DNS data to obtain the profile for W_D. This readily constitutes the model S_L^IM while the model $S_\mathrm{L}^\mathrm{OGM}$ is obtained by multiplying with 0.75. For the models S_L^PB and $S_\mathrm{L}^\mathrm{Lahey}$, where the prefactor of W_D is not constant according to Table 2, C_D and α_L are determined from the DNS data as well. This procedure, which fully relies on the DNS data for model evaluation, is denoted as *a priori* testing. Fig. 4 shows that the curves for S_L^PB strongly overestimate the DNS data for all three cases. The curves for S_L^IM and $S_\mathrm{L}^\mathrm{OGM}$ differ only by the value of the constant prefactor, with $S_\mathrm{L}^\mathrm{OGM}$ being overall in slightly better agreement with the DNS data. The curves for $S_\mathrm{L}^\mathrm{Lahey}$ overestimate the DNS profiles in some regions and underestimate it in other regions. By considering Fig. 4 (a)-(c), the models of Olmos, Gentric, and Midoux [50] and Lahey [51] are selected for further testing in EE simulations.

4. Euler-Euler simulations of a pilot-scale bubble column

This section presents the governing equations, the computational set-up and the results for the EE RANS simulations of an industrial pilot-scale bubble column under isothermal conditions. Similar to the DNS, both phases are considered to be incompressible and immiscible.

4.1. Two-fluid model

For the EE simulations, the top-level solver *twoPhaseEulerFoam* is used that is frequently employed to study flows in bubble columns [12, 53, 54]. The code solves the conditionally averaged (ca) continuity and momentum equations in the following form

$$\frac{\partial}{\partial t}(\alpha_i\rho_i) + \nabla \cdot (\alpha_i\rho_i\mathbf{u}_i^\mathrm{ca}) = 0, \tag{9}$$
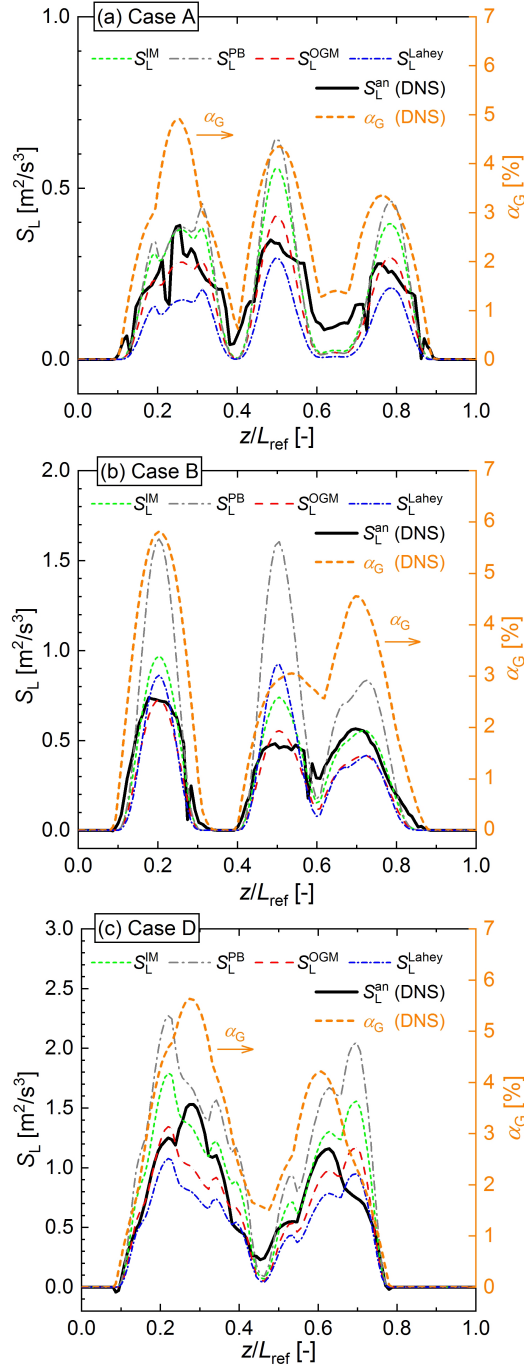
12

Figure 4: *A priori* testing of models for the interfacial term: (a) Case A, (b) Case B, (c) Case D. For each case, the analytical profile S_L^{an} evaluated from the DNS data is compared with profiles predicted by the four models in Table 2.

$$\frac{\partial}{\partial t}(\alpha_i \rho_i \mathbf{u}_i^{\mathrm{ca}}) + \nabla \cdot (\alpha_i \rho_i \mathbf{u}_i^{\mathrm{ca}} \mathbf{u}_i^{\mathrm{ca}}) = -\alpha_i \nabla p^{\mathrm{ca}} + \nabla \cdot (\alpha_i \rho_i \mathbb{R}_i^{\mathrm{eff}}) + \alpha_i \rho_i \mathbf{g} + \mathbf{F}_i^{\mathrm{int}}. \quad (10)$$

Here, α_i is the volume fraction and $\mathbf{u}_i^{\mathrm{ca}}$ is the (conditionally averaged) velocity of phase $i \in \{\mathrm{G}, \mathrm{L}\}$ while p^{ca} denotes the pressure field shared by both phases.

The term $\mathbf{F}_i^{\mathrm{int}}$ accounts for the average effect of the forces acting at the interface between continuous and dispersed phase due to their relative motion. In their baseline model for monodisperse flows, Rzehak et al. [55] considered in addition to the drag force ($\mathbf{F}_{\mathrm{D}}$), the lift force ($\mathbf{F}_{\mathrm{Lift}}$), the virtual mass force ($\mathbf{F}_{\mathrm{VM}}$), the turbulent dispersion dispersion force ($\mathbf{F}_{\mathrm{TD}}$), and the wall force ($\mathbf{F}_{\mathrm{W}}$) so that

$$\mathbf{F}_{\mathrm{G}}^{\mathrm{int}} = -\mathbf{F}_{\mathrm{L}}^{\mathrm{int}} = \mathbf{F}_{\mathrm{D}} + \mathbf{F}_{\mathrm{Lift}} + \mathbf{F}_{\mathrm{VM}} + \mathbf{F}_{\mathrm{TD}} + \mathbf{F}_{\mathrm{W}}. \quad (11)$$

For a mathematical representation of these forces and common models we refer to [11]. Since $C_{\mathrm{D}}^{\mathrm{To}}$ from Eq. (8) resulted in convergence issues, the Schiller-Naumann drag coefficient $C_{\mathrm{D}}^{\mathrm{SN}} = 24(1 + 0.15 Re_{\mathrm{B}}^{0.687})/Re_{\mathrm{B}}$ is used in combination with the swarm correction of Tomiyama, see [11, Table 2]. The coefficient in the virtual mass force is set to 0.5 while the lift coefficient is modelled according to Legendre and Magnaudet [56]. For the turbulent dispersion force, the model proposed by Lahey et al. [57] is used with coefficient $C_{\mathrm{TD}} = 0.5$. Similar to [58], the wall force is neglected here.

The effective stress tensor $\mathbb{R}_i^{\mathrm{eff}} = \mathbb{R}_i^{\mathrm{mol}} + \mathbb{R}_i^{\mathrm{turb}}$ includes molecular and turbulent stresses. Reynolds stresses are modelled by the eddy viscosity concept. Instead of a per phase turbulence model, the mixture turbulence model proposed in [59, 60] is used here. In this approach, Reynolds stresses of the continuous phase are given by

$$\mathbb{R}_{\mathrm{L}}^{\mathrm{turb}} = \nu_{\mathrm{L}}^{\mathrm{turb}} \left(\nabla \mathbf{u}_{\mathrm{L}}^{\mathrm{ca}} + (\nabla \mathbf{u}_{\mathrm{L}}^{\mathrm{ca}})^{\mathsf{T}}\right) - \frac{2}{3} k_{\mathrm{L}} \mathbb{I} \quad (12)$$

while Reynolds stresses of the dispersed phase are directly related to those of the continuous phase by $\mathbb{R}_{\mathrm{G}}^{\mathrm{turb}} = C_{\mathrm{t}}^2 \mathbb{R}_{\mathrm{L}}^{\mathrm{turb}}$. Here, $C_{\mathrm{t}} = C_{\mathrm{t}}(d_{\mathrm{B}}, \alpha_{\mathrm{G}}, \rho_{\mathrm{G}}/\rho_{\mathrm{L}}, ...)$ is a rather complicated turbulence response function, see [60, Sect. 4.2] for details. The turbulent viscosity of the continuous phase is computed as

$$\nu_{\mathrm{L}}^{\mathrm{turb}} = C_\mu \frac{k_{\mathrm{m}}^2}{\varepsilon_{\mathrm{m}}}, \quad (13)$$

where k_{m} and ε_{m} denote the mixture turbulence kinetic energy and its dissipation rate. For both quantities, transport equations are solved [60]. The

transport equation for k_m reads

$$\frac{\partial}{\partial t}(\rho_\mathrm{m} k_\mathrm{m}) + \nabla \cdot (\rho_\mathrm{m} k_\mathrm{m} \mathbf{u}_\mathrm{m}^\mathrm{ca}) = \nabla \cdot \left(\frac{\mu_\mathrm{m}^\mathrm{turb}}{\sigma_k} \nabla k_\mathrm{m} \right) + P_\mathrm{m}^\mathrm{md} - \rho_\mathrm{m} \varepsilon_\mathrm{m} + S_\mathrm{m}^\mathrm{md}, \quad (14)$$

where $P_\mathrm{m}^\mathrm{md} = \alpha_\mathrm{L} P_\mathrm{L}^\mathrm{md} + \alpha_\mathrm{G} P_\mathrm{G}^\mathrm{md}$. For the present computations, where $\rho_\mathrm{G} \ll \rho_\mathrm{L}$ and the gas holdup is low, it is $\rho_\mathrm{m} \approx \rho_\mathrm{L}$, $k_\mathrm{m} \approx k_\mathrm{L}$ and $\varepsilon_\mathrm{m} \approx -\varepsilon_\mathrm{L}$ (due to the definitions with opposite signs, cf. Eq. 5). Similar to [58], the five coefficients of the turbulence model (including $C_\mu = 0.09$ and $\sigma_k = 1.0$) are set to standard single-phase values [61]. The interfacial source term in Eq. (14) is approximated as $S_\mathrm{m}^\mathrm{md} \approx S_\mathrm{L}^\mathrm{md}$. For S_L^md, the models of Olmos et al. [50] and Lahey [51] (cf. Table 2) are used in the EE simulations, which were found to perform best in the *a priori* tests against the DNS data.

4.2. Set-up and procedures

For the present simulations, an industrial pilot-scale bubble column at Evonik Industries AG (Marl, Germany) operated at pressures of up to 36 bar and temperatures of up to 75°C is considered [6, 7]. The diameter and height of the stainless steel bubble column are $D_\mathrm{BC} = 0.33$ m and $H_\mathrm{BC} = 5$ m, respectively. The initial liquid height measured from the bottom of the column is $H_\mathrm{L} = 3.88$ m corresponding to $H_\mathrm{L}/D_\mathrm{BC} = 11.76$. The geometry of the bubble column is displayed in Fig. 5 (a). A sketch of the entire test facility and instrumentation is provided in [6, Fig. 3]. Gas (nitrogen) and liquid (cumene or deionized water) are operated in co-current upward flow. The gas is introduced in the lower part of the column by a perforated plate sparger (240 mm in diameter with 352 circular holes each 1 mm in diameter, free area 0.65%) and leaves the column at the top. Liquid is circulated by a pump entering the column at the bottom through a single tubular inlet (diameter 24 mm) and leaving it at the top. Experiments were performed with a gas superficial velocity (U_G^0) up to 5 cm/s at low superficial liquid velocities (U_L^0) of 0.8 and 1.8 cm/s. Measurements in [6] focus on the effects of liquid phase and operational conditions on overall gas holdup (ϵ_G), while in [7] the focus is on distributions of bubble size and bubble velocity. For cumene, bubble sizes were measured in the range $0.5 - 5$ mm corresponding to $Eo \approx 0.3 - 10$.

The meshed geometrical representation of the bubble column for the EE simulations was provided by Evonik Industries AG. Fig. 5 (a) shows a perspective view of the computational domain which is discretized by an unstructured mesh (polyMesh). The cross-section of the main cylindrical part
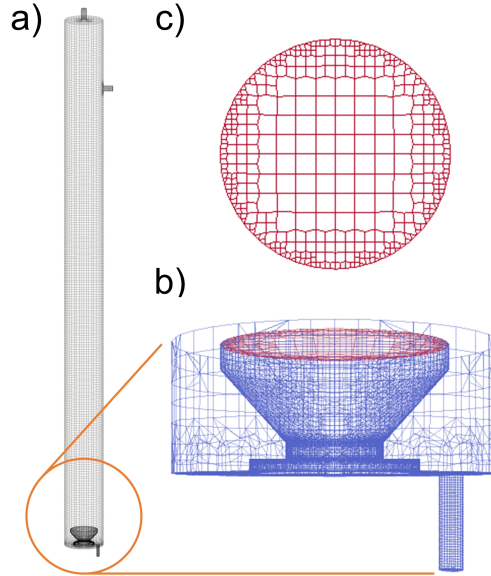
Figure 5: Geometry and mesh of the bubble column. (a) Perspective view of the entire BC, (b) Detail of the bottom part showing the tubular liquid inlet, the sparger geometry and the gas inlet (red), (c) Meshing of the gas inlet.

of the bubble column is discretized by 18×18 mesh cells while in vertical direction 263 mesh cells are used. Fig. 5 (b) shows the lower part of the BC with liquid inlet and sparger. The mesh for the gas inlet is displayed in Fig. 5 (c). As initial conditions, the lower part of the bubble column up to the liquid outlet at height H_L is filled by liquid ($\alpha_L = 1$), while the part above is filled with gas ($\alpha_G = 1$), both phases being at rest. For $t > 0$, constant flow rates of gas and liquid (cf. Table 3) enter through the sparger and the liquid inlet, respectively. The calculation of values for k and ε at the gas and liquid inlets is explained in Appendix A. For details on the modeling of the sparger we refer to [17, Sect 5.1.3].

For both liquids, a large number of EE simulations have been performed under varying system pressures (1, 18.5 and 36 bar) and temperatures (23 and 70°C) [43, Table 10]. Monodisperse conditions are always assumed and only selected results will be presented here. For water ($T = 23$°C), the bubble diameter is 4.0 mm at 1 bar in accordance to the peak of the bubble size distribution measured in [37] while $d_B = 2.25$ mm is used for the two elevated pressure levels. For cumene ($T = 70$°C), a bubble diameter $d_B \approx 2.9$ mm

16

is used for all pressure levels corresponding to the Sauter mean diameter measured in [7]. The physical properties used in the simulations are listed in Table 3; they are similar to those given in [6, 7].

Table 3: Parameters used in EE simulations for liquid phases water ($T = 23°C$) and cumene ($T = 70°C$) with gas phase nitrogen.

Liquid phase	p bar	d_B mm	U_L^0 cm/s	U_G^0 cm/s	ρ_L kg/m^3	ρ_G kg/m^3	μ_L mPa s	μ_G mPa s	σ mN/m
Water	1.0	4.0	0.84	0.56	997.1	1.13	0.850	0.0178	71.5
	18.5	2.25	0.84	0.55	997.8	20.9	0.850	0.0181	68.7
	36.0	2.25	0.84	0.55	998.6	40.8	0.850	0.0184	67.1
Cumene	1.0	2.93	0.82	0.68	820.5	0.97	0.427	0.0198	26.0
	18.5	2.94	0.82	0.61	825.9	17.8	0.427	0.0201	25.5
	36.0	2.94	0.82	0.54	828.7	34.6	0.427	0.0204	25.2

4.3. Results

This section presents selected results of EE simulations for the cases listed in Table 3. First, the overall flow structure in the bubble column is illustrated by visualizing the gas content. Next, radial profiles of α_G are compared with measurements. This is followed by radial profiles for turbulence kinetic energy before finally results for overall gas holdup are compared with empirical correlations.

4.3.1. Flow structure

Fig. 6 displays the gas content in the vertical center plane of the bubble column for the six cases listed in Table 3 at the end of each simulation. In the simulations, the model of Lahey is used if not mentioned otherwise. For the water cases at 18.5 and 36 bar, a steady state is achieved after 390 s. Illustrations of the transient process for water at 18.5 bar toward the steady state can be found in [43, Fig. 40]. For water at 1 bar, no steady state is achieved instead. The reason could be related to the larger bubble diameter of 4 mm as compared with 2.25 mm at elevated pressures. With larger diameter, bubbles rise much faster and appropriate modeling of the lift force becomes an issue as the lift coefficient may change sign [62]. For cumene, no steady state is achieved for any of the three pressure levels. However, in all cases without strict steady state, a quasi-steady state is achieved after an initial transient. In this quasi-steady state, slight spatial and temporal fluctuations around time-independent mean values are observed for various
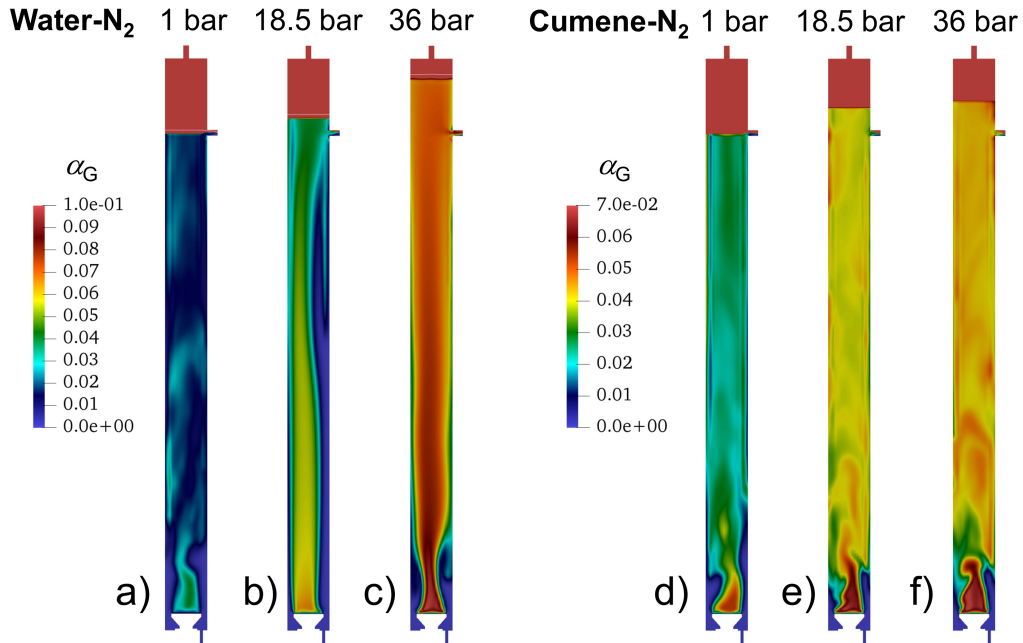
17

Figure 6: Gas distribution in a vertical midplane illustrating the flow structure in the bubble column.

quantities including α_{G}. Results for water at 1 bar and for cumene to be presented in subsequent sections have therefore been obtained by transient averaging over the quasi-steady time period.

As can be seen in Fig. 6, the conditions in the vicinity of the sparger are notably influenced by the lateral liquid feed which breaks the axial symmetry of the BC. For this reason, the gas distribution in the lower quarter of the bubble column is not radially symmetric. At higher elevations, the gas distribution is approximately radially symmetric (with higher values in the middle and lower values near the wall) with exception of the water case at 18.5 bar. For this case, a liquid recirculation region with very low gas content is formed with the gas plume leaning against the other side of the BC. For both liquids, a significant increase of the overall gas content with system pressure can be deduced from Fig. 6 in agreement with measurements [6, Fig. 19], going along with the increase of liquid level in Fig. 6.

18
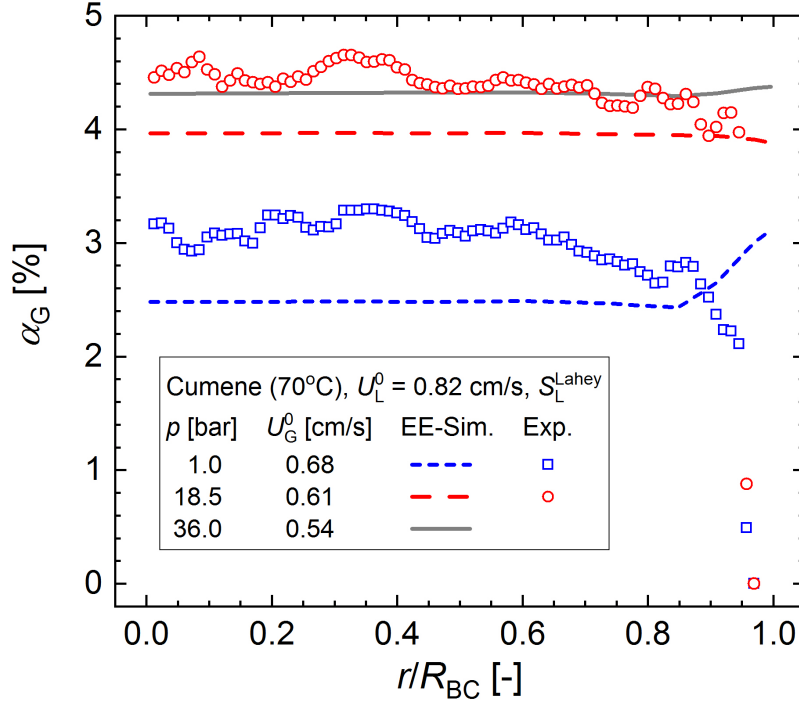
Figure 7: Radial profiles of α_G for cumene-nitrogen system at different pressures in a horizontal cross-section at height 2.23 m (about the middle of the bubble column). Comparison of present EE simulations (lines) with experimental results [6, 37] (symbols). The radial coordinate is normalized by the bubble column radius ($R_{BC} = 165$ mm).

4.3.2. Local gas holdup

Contour plots for gas holdup in a horizontal cross section at height 2.23 m are averaged in azimuthal direction and in time to obtain radial profiles $\alpha_G(r)$. In Fig. 7, the profiles for cumene are compared with experimental profiles from [6, 37], measured by high-resolution gamma ray computed tomography [63] and wire-mesh sensors [64]. Both, in experiment and simulation, the profiles are quite flat indicating a (beneficial) rather uniform gas distribution across the bubble column. In the experiment, the local gas content strongly decreases near the wall, an effect not observed in the simulations as these are performed without wall lubrication force. Quantitatively, the EE simulations underestimate the experimental values of α_G in the core region by about 15% at 1 bar, and by approximately 10% at 18.5 bar. As the gas superficial velocity (U_G^0) is identical in experiment and simulation for

19

each pressure level, the underestimation of α_G in the simulation goes along with an overestimation of gas velocity. In the simulations, an increase of local gas holdup with system pressure is observed despite the decrease of U_G^0. This can be attributed to the decrease of the buoyancy force with system pressure which results in a decrease of bubble rise velocity.

For water simulations, radial profiles of α_G are less uniform and exhibit a more parabolic shape even in the absence of the wall lubrication force. While this behaviour is in qualitative agreement with measurements, the quantitative comparison with experimental α_G profiles in water is less satisfactorily [43, Sec. 5.2.3]. Despite the rather large differences in local gas holdup for both liquids, the radial profiles of computed mean gas and liquid velocity are quite similar for cumene and water.

4.3.3. Turbulence kinetic energy

Similar to the procedure in Section 4.3.2, results for the local turbulence kinetic energy in a cross-section at 2.23 m height are averaged in the azimuthal direction (and for cumene over time) to obtain radial profiles $k_m(r)$. For water at 18.5 bar, the effect of the interfacial term is studied by performing simulations not only with the Lahey model [51] but also with the OGM [50] model. To test the sensitivity of k_m with respect to the model for S_L^{an}, one additional EE simulation is performed where the prefactor in the Lahey model is doubled arbitrarily.

The radial profiles of k_m for water and cumene at various pressures are displayed in Fig. 8. In all cases, the profiles are quite flat. For water at 18.5 bar, the profiles obtained with the OGM and Lahey models are very similar and differences are small. Doubling the prefactor of the Lahey model increases k_m by about a factor of 2.2, indicating an almost linear increase of k_m at this pressure. An increase of system pressure from 18.5 to 36 bar decreases k_m by about a factor of two for water. A similar decrease of k_m with system pressure is observed for cumene. For cumene, values of k_m are notably smaller as compared with water, though physical properties and bubble diameter are quite similar for both elevated system pressures. This may be attributed to the lower Morton number of cumene in comparison with water.

The radial profiles for k_m in Fig. 8 and those for α_G in Fig. 7 are almost uniform over a wide part of the BC cross section. For the development of algebraic models for bubble-induced turbulence [24], relations between local turbulent kinetic energy and quantities such as local gas content and gas
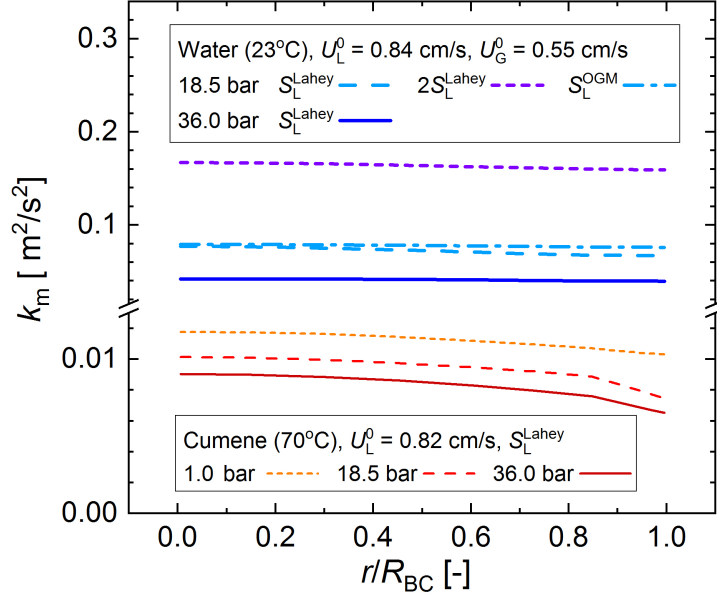
20

Figure 8: Radial profiles of k_m in a horizontal cross-section at height 2.23 m. Note that for cumene, the gas superficial velocity slightly differs with system pressure, see Table 3.

velocity are of interest. Fig. 9 shows a plot of k_m versus the square of the local superficial gas velocity given by the product between local gas content and local vertical gas velocity ($u_{\mathrm{G},z}$). For each EE case, ten data points are displayed each representing the azimuthal average at a certain radial position at height 2.23 m. The radial positions extend from $r = 1$ mm close to the BC centerline to $r = 164$ mm close to the BC wall (located at 165 mm). The cumene data for different pressure levels scatter close to the wall. However, away from the wall ($r \leq 150$ mm) the data almost collapse to a single curve indicating a linear dependence of k_m on the square of the local superficial gas velocity, a relation which is (with much smaller slope) also observed for the water case.

4.3.4. Overall gas holdup

For the design of bubble column reactors, precise prediction of the overall gas holdup (ϵ_G) is essential. While a vast number of correlations exist for that purpose, only the Zehner [65] correlation was found to predict the trends observed in the experiments by Rollbusch et al. [6]. The empirical correlation
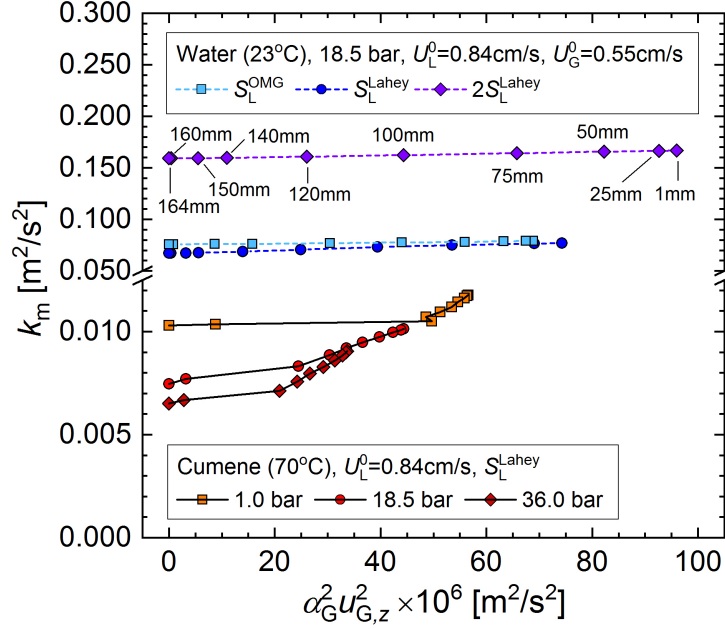
21

Figure 9: Mixture turbulence kinetic energy versus square of local superficial gas velocity. Azimuthally averaged data for ten different radial positions at height 2.23 m. For each case, the sequence of the individual symbols corresponds to the radial positions indicated for water case with model $2S_\mathrm{L}^\mathrm{Lahey}$.

of Zehner [65] reads

$$\epsilon_\mathrm{G}^\mathrm{emp} = \frac{U_\mathrm{G}^0}{U_\mathrm{B}^\mathrm{slip}} \left[1 + 4 \frac{U_\mathrm{L}^\mathrm{cl}}{U_\mathrm{B}^\mathrm{slip}} \left(\frac{U_\mathrm{G}^0}{U_\mathrm{B}^\mathrm{slip}} \right)^{2/3} \right]^{-0.5}. \tag{15}$$

Here, U_L^cl is the maximum center-line velocity of the liquid given by

$$U_\mathrm{L}^\mathrm{cl} = \sqrt[3]{0.4(1 - \rho_\mathrm{G}/\rho_\mathrm{L})gU_\mathrm{G}^0 D_\mathrm{BC}}. \tag{16}$$

In Eq. (15), $U_\mathrm{B}^\mathrm{slip}$ is the slip velocity of the biggest stable single bubble. Different correlations for this velocity have been proposed in literature. Here, the relation

$$U_\mathrm{B}^\mathrm{slip} = C_\mathrm{B}^\mathrm{slip} \sqrt[4]{\frac{\sigma g(\rho_\mathrm{L} - \rho_\mathrm{G})}{\rho_\mathrm{L}^2}} \tag{17}$$
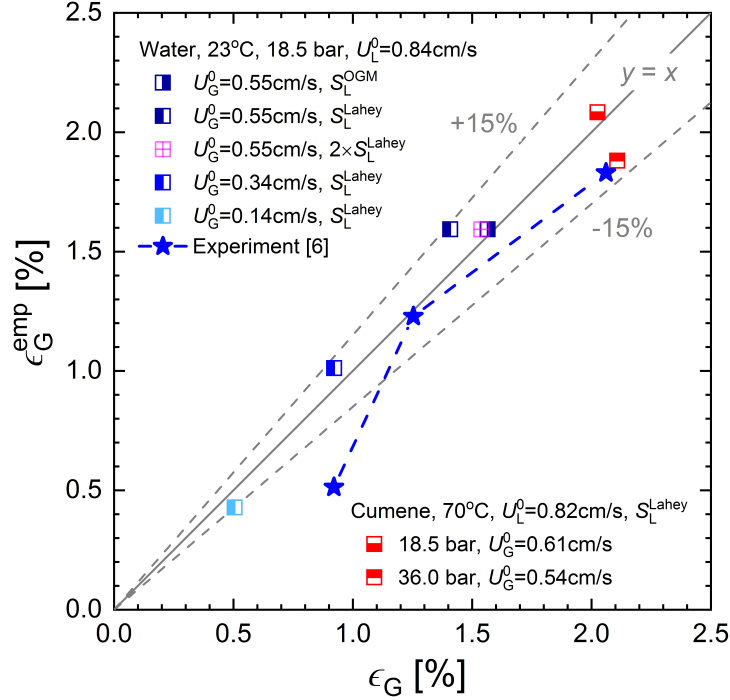
22

Figure 10: Comparison of measured/computed overall gas holdup (abscissa) with empirical correlation ϵ_G^{emp} of Zehner [65] in combination with the slip velocity from Mersmann [66]. Values of U_G^0 in the experiment are 0.169, 0.417 and 0.639 cm/s, respectively.

is used in combination with $C_B^{\text{slip}} = 2$ as proposed by Mersmann [66] while a prefactor $C_B^{\text{slip}} = 1.55$ is recommended in [6].

Fig. 10 compares the overall gas holdup as evaluated from the present EE computations with measurements [6] and the correlation given by Eqs. (15)–(17) using a parity plot. In addition to the cases listed in Table 3, results from two additional water simulations with reduced gas superficial velocity are included [43]. For water and $U_G^0 = 0.55$ cm/s, a certain influence of the choice for S_L^{md} can be identified. With the OGM model, the simulation results are very close to the parity line. For the Lahey model, the value of ϵ_G is lower and the deviation from the parity line is larger. However, by doubling the coefficient in the Lahey model, the value of ϵ_G increases and becomes close to that obtained with the OGM model. Overall, the simulation results for water at 18.5 bar and for cumene system at 18.5 and 36 bar are predicted quite well by the Zehner correlation [65] with a deviation below 15%.

23

5. Conclusions

This study presents numerical investigations of bubbly two-phase flows on various scales to test closure relations for bubble-induced turbulence. On the bubble swarm scale, direct numerical simulations with a volume-of-fluid method are performed considering a sub-region of a flat bubble column with void fractions of about 2%. The main findings of the DNS study can be summarized as follows: (i) The evaluation of the analytical budget of the turbulence kinetic energy (TKE) shows that the interfacial term is the main source term while production by shear is negligible for the conditions investigated in this study. (ii) In the TKE budget, there is no local equilibrium between interfacial production and dissipation. Instead, diffusion redistributes the surplus of TKE existing in regions with high void fraction towards the regions with low void fraction. (iii) By comparison with the DNS data, the *a priori* performance of four models from literature for closure of the interfacial term are evaluated, and the models of Olmos, Gentric, and Midoux [50] and Lahey [51] are identified for further testing.

For an industrial pilot-scale bubble column (with 330 mm diameter and 5 m height), Euler-Euler RANS computations are performed using the Open-FOAM solver *twoPhaseEulerFoam*. Turbulence is modeled by an eddy viscosity concept employing a mixture k_m-ε_m model in combination with the Lahey model for the interfacial term. Simulations are performed for two different liquids (water and cumene) at three different pressure levels (1, 18.5 and 36 bar). Radial gas holdup profiles in the middle of the bubble column are compared with experiments. The numerical results for cumene are well aligned with measurements deviating less than 15%, while for water the deviation is somewhat larger.

Radial profiles of k_m are quite flat for all cases. For both liquids, a decrease of k_m with system pressure is observed. For a given pressure, values of k_m in water are about a factor of $5-8$ higher as compared with cumene. For water at 18.5 bar, the influence of the model for the interfacial term is tested. Differences between the model of Lahey and the one of Olmos, Gentric, and Medoux are small, in general . An arbitrary doubling of the prefactor of the Lahey model increases k_m slightly disproportionately, highlighting the importance of determining the prefactor properly. The influence on the overall gas holdup (ϵ_G) in the bubble column is, however, quite small. Simulation results for ϵ_G are compared with an empirical model based on a correlation combining proposals by Zehner and by Mersmann. A deviation

of maximum 15% indicates that the empirical model is well suited to predict ϵ_G for cumene and water at elevated pressures for the present conditions.

Overall, the presented systematic approach provides a framework for the development of improved statistical turbulence models for bubble-driven liquid flows, which are essential for the advancement of CFD as a tool for design of industrial bubble columns.

Acknowledgements

Appendix A. Turbulence boundary conditions at inlets

The EE simulations require values for k and ε at the gas and liquid inlets as boundary conditions. Table A1 summarizes these values for the EE simulations in Table 3. As detailed in [43, Sect. 5.1.3], values for k have been computed as $k = 0.5U_{\mathrm{mean}}^2 T_{\mathrm{i}}^2$ with turbulence intensity $T_{\mathrm{i}} = 0.16Re_{\mathrm{D_h}}^{-1/8}$ as suggested for pipe flows with Reynolds number ($Re_{D_{\mathrm{h}}}$) being based on the hydraulic diameter (D_{h}). Here, the hydraulic diameter of the liquid inlet is $D_{\mathrm{h}} = 24$ mm. For the gas inlet, the diameter of the sparger holes is used ($D_{\mathrm{h}} = 1$ mm). The dissipation rate is determined as $\varepsilon = C_\mu^{3/4}k^{3/2}/l$, where $l = 0.07D_{\mathrm{h}}$.

Table A1: Boundary conditions for k and ε at BC inlets.

Liquid phase	p bar	Liquid inlet		Gas inlet	
		k m²/s²	ε m²/s³	k m²/s²	ε m²/s³
Water	1.0	0.0043	0.027	0.023	8.23
	18.5	0.0043	0.027	0.010	2.63
	36.0	0.0043	0.027	0.092	2.07
Cumene	1.0	0.0036	0.022	0.035	15.1
	18.5	0.0036	0.022	0.014	3.82
	36.0	0.0036	0.022	0.0095	2.18

References

[1] N. Kantarci, F. Borak, K. O. Ulgen, Bubble column reactors, Process Biochemistry 40 (2005) 2263–2283. doi:10.1016/j.procbio.2004.10.004.

[2] G. Besagni, F. Inzoli, T. Ziegenhein, Two-phase bubble columns: A comprehensive review, ChemEngineering 2 (2018) 13. doi:10.3390/chemengineering2020013.

[3] A. Shaikh, M. H. Al-Dahhan, A review on flow regime transition in bubble columns, International Journal of Chemical Reactor Engineering 5 (2007). doi:10.2202/1542-6580.1368.

[4] P. Rollbusch, M. Bothe, M. Becker, M. Ludwig, M. Grünewald, M. Schlüter, R. Franke, Bubble columns operated under industrially relevant conditions – current understanding of design parameters, Chemical Engineering Science 126 (2015) 660–678. doi:10.1016/j.ces.2014.11.061.

[5] R. S. Abdulmohsin, B. A. Abid, M. H. Al-Dahhan, Heat transfer study in a pilot-plant scale bubble column, Chemical Engineering Research and Design 89 (2011) 78–84. doi:10.1016/j.cherd.2010.04.019.

[6] P. Rollbusch, M. Becker, M. Ludwig, A. Bieberle, M. Grünewald, U. Hampel, R. Franke, Experimental investigation of the influence of column scale, gas density and liquid properties on gas holdup in bubble columns, International Journal of Multiphase Flow 75 (2015) 88–106. doi:10.1016/j.ijmultiphaseflow.2015.05.009.

[7] M. Bothe, M.-A. Christlieb, M. Hoffmann, O. Tedjasukmana, F. Michaux, P. Rollbusch, M. Becker, M. Schlüter, Bubble size and bubble velocity distribution in bubble columns under industrial conditions, The Canadian Journal of Chemical Engineering 95 (2017) 902–912. doi:10.1002/cjce.22759.

[8] H. A. Jakobsen, H. Lindborg, C. A. Dorao, Modeling of bubble column reactors: Progress and limitations, Industrial & Engineering Chemistry Research 44 (2005) 5107–5151. doi:10.1021/ie049447x.

[9] C. Laborde-Boutet, F. Larachi, N. Dromard, O. Delsart, D. Schweich, CFD simulation of bubble column flows: Investigations on turbulence

26

models in RANS approach, Chemical Engineering Science 64 (2009) 4399–4413. doi:10.1016/j.ces.2009.07.009.

[10] D. F. Fletcher, D. D. McClure, J. M. Kavanagh, G. W. Barton, CFD simulation of industrial bubble columns: Numerical challenges and model validation successes, Applied Mathematical Modelling 44 (2017) 25–42. doi:10.1016/j.apm.2016.08.033.

[11] A. Mühlbauer, M. W. Hlawitschka, H.-J. Bart, Models for the numerical simulation of bubble columns: A review, Chemie Ingenieur Technik 91 (2019) 1747–1765. doi:10.1002/cite.201900109.

[12] V. Kannan, P. R. Naren, V. V. Buwa, A. Dutta, Effect of drag correlation and bubble-induced turbulence closure on the gas hold-up in a bubble column reactor, Journal of Chemical Technology & Biotechnology 94 (2019) 2944–2954. doi:10.1002/jctb.6100.

[13] A. Vaidheeswaran, T. Hibiki, Bubble-induced turbulence modeling for vertical bubbly flows, International Journal of Heat and Mass Transfer 115 (2017) 741–752. doi:10.1016/j.ijheatmasstransfer.2017.08.075.

[14] M. Lance, J. Bataille, Turbulence in the liquid phase of a uniform bubbly air–water flow, Journal of Fluid Mechanics 222 (1991) 95–118. doi:10.1017/S0022112091001015.

[15] F. Risso, K. Ellingsen, Velocity fluctuations in a homogeneous dilute dispersion of high-Reynolds-number rising bubbles, Journal of Fluid Mechanics 453 (2002) 395–410. doi:10.1017/S0022112001006930.

[16] I. Roghair, J. M. Mercado, M. V. Sint Annaland, H. Kuipers, C. Sun, D. Lohse, Energy spectra and bubble velocity distributions in pseudo-turbulence: Numerical simulations vs. experiments, International Journal of Multiphase Flow 37 (2011) 1093–1098. doi:10.1016/j.ijmultiphaseflow.2011.07.004.

[17] A. Serizawa, I. Kataoka, I. Michiyoshi, Turbulence structure of air-water bubbly flow—II. Local properties, International Journal of Multiphase Flow 2 (1975) 235–246. doi:10.1016/0301-9322(75)90012-9.

[18] T. Ma, D. Lucas, S. Jakirlić, J. Fröhlich, Progress in the second-moment closure for bubbly flow based on direct numerical simulation data, Journal of Fluid Mechanics 883 (2020) A9. doi:10.1017/jfm.2019.851.

[19] T. Ziegenhein, R. Rzehak, T. Ma, D. Lucas, Towards a unified approach for modelling uniform and non-uniform bubbly flows, The Canadian Journal of Chemical Engineering 95 (2017) 170–179. doi:10.1002/cjce.22647.

[20] T. Ma, C. Santarelli, T. Ziegenhein, D. Lucas, J. Fröhlich, Direct numerical simulation–based Reynolds-averaged closure for bubble-induced turbulence, Phys. Rev. Fluids 2 (2017) 034301. doi:10.1103/PhysRevFluids.2.034301.

[21] B. Magolan, E. Baglietto, Assembling a bubble-induced turbulence model incorporating physical understanding from DNS, International Journal of Multiphase Flow 116 (2019) 185–202. doi:10.1016/j.ijmultiphaseflow.2019.04.009.

[22] S. Shu, N. El Bahraoui, F. Bertrand, J. Chaouki, A bubble-induced turbulence model for gas-liquid bubbly flows in airlift columns, pipes and bubble columns, Chemical Engineering Science 227 (2020) 115945. doi:10.1016/j.ces.2020.115945.

[23] N. Panicker, A. Passalacqua, R. Fox, Computational study of buoyancy driven turbulence in statistically homogeneous bubbly flows, Chemical Engineering Science 216 (2020) 115546. doi:10.1016/j.ces.2020.115546.

[24] T. Ma, D. Lucas, A. D. Bragg, Explicit algebraic relation for calculating Reynolds normal stresses in flows dominated by bubble-induced turbulence, Phys. Rev. Fluids 5 (2020) 084305. doi:10.1103/PhysRevFluids.5.084305.

[25] S. Hosokawa, T. Suzuki, A. Tomiyama, Turbulence kinetic energy budget in bubbly flows in a vertical duct, Experiments in Fluids 52 (2012) 719–728. doi:10.1007/s00348-011-1109-z.

[26] J. Lu, G. Tryggvason, Dynamics of nearly spherical bubbles in a turbulent channel upflow, Journal of Fluid Mechanics 732 (2013) 166–189. doi:10.1017/jfm.2013.397.

[27] B. Magolan, E. Baglietto, C. Brown, I. A. Bolotnov, G. Tryggvason, J. Lu, Multiphase turbulence mechanisms identification from consistent analysis of direct numerical simulation data, Nuclear Engineering and Technology 49 (2017) 1318–1325. doi:10.1016/j.net.2017.08.001.

[28] J. Hasslberger, M. Klein, N. Chakraborty, Flow topologies in bubble-induced turbulence: a direct numerical simulation analysis, Journal of Fluid Mechanics 857 (2018) 270–290. doi:10.1017/jfm.2018.750.

[29] G. Grötzbach, M. Wörner, Direct numerical and large eddy simulations in nuclear applications, International Journal of Heat and Fluid Flow 20 (1999) 222–240. doi:10.1016/S0142-727X(99)00012-0.

[30] M. Wörner, G. Grötzbach, Pressure transport in direct numerical simulations of turbulent natural convection in horizontal fluid layers, International Journal of Heat and Fluid Flow 19 (1998) 150–158. doi:10.1016/S0142-727X(97)10019-4.

[31] M. Ilic, Statistical analysis of liquid phase turbulence based on direct numerical simulations of bubbly flows, Ph.D. thesis, Universität Karlsruhe (TH), 2005. doi:10.5445/IR/1000004371.

[32] M. Ilic, M. Wörner, D. G. Cacuci, Balance of liquid-phase turbulence kinetic energy equation for bubble-train flow, Journal of Nuclear Science and Technology 41 (2004) 331–338. doi:10.1080/18811248.2004.9715492.

[33] M. Wörner, B. E. Ghidersa, M. Ilic, D. G. Cacuci, Volume-of-fluid method based numerical simulations of gas-liquid two-phase flow in confined geometries, La Houille Blanche (2005) 91–104. doi:10.1051/lhb:200506008.

[34] C. Santarelli, J. Fröhlich, Direct numerical simulations of spherical bubbles in vertical turbulent channel flow. Influence of bubble size and bidispersity, International Journal of Multiphase Flow 81 (2016) 27–45. doi:10.1016/j.ijmultiphaseflow.2016.01.004.

[35] C. Santarelli, J. Roussel, J. Fröhlich, Budget analysis of the turbulent kinetic energy for bubbly flow in a vertical channel, Chemical Engineering Science 141 (2016) 46–62. doi:10.1016/j.ces.2015.10.013.

[36] J. Feng, I. A. Bolotnov, Evaluation of bubble-induced turbulence using direct numerical simulation, International Journal of Multiphase Flow 93 (2017) 92–107. doi:10.1016/j.ijmultiphaseflow.2017.04.003.

[37] A. Bieberle, M. Schubert, P. Rollbusch, M. Becker, E. Schleicher, U. Hampel, Tomographic imaging of gas holdup distribution in pressurized bubble columns, in: Proceedings of the 2nd International Symposium on Multiscale Multiphase Process Engineering (MMPE), 2014, pp. 262–267.

[38] W. Sabisch, M. Wörner, G. Grötzbach, D. G. Cacuci, Dreidimensionale numerische Simulation von aufsteigenden Einzelblasen und Blasenschwärmen mit einer Volume-of-Fluid-Methode, Chemie Ingenieur Technik 73 (2001) 368–373. doi:10.1002/1522-2640(200104)73:4<368::AID-CITE368>3.0.CO;2-W.

[39] M. C. Öztaskin, M. Wörner, H. S. Soyhan, Numerical investigation of the stability of bubble train flow in a square minichannel, Physics of Fluids 21 (2009) 042108. doi:10.1063/1.3101146.

[40] Ö. Keskin, M. Wörner, H. S. Soyhan, T. Bauer, O. Deutschmann, R. Lange, Viscous co-current downward Taylor flow in a square minichannel, AIChE Journal 56 (2010) 1693–1702. doi:10.1002/aic.12113.

[41] H. Marschall, S. Boden, C. Lehrenfeld, C. J. Falconi, U. Hampel, A. Reusken, M. Wörner, D. Bothe, Validation of interface capturing and tracking techniques with different surface tension treatments against a Taylor bubble benchmark problem, Computers & Fluids 102 (2014) 336–352. doi:10.1016/j.compfluid.2014.06.030.

[42] C. J. Falconi, C. Lehrenfeld, H. Marschall, C. Meyer, R. Abiev, D. Bothe, A. Reusken, M. Schlüter, M. Wörner, Numerical and experimental analysis of local flow phenomena in laminar Taylor flow in a square minichannel, Physics of Fluids 28 (2016) 012109. doi:10.1063/1.4939498.

[43] S. Erdogan, Numerical analysis and modelling of liquid turbulence in bubble columns at various scales by Computational Fluid Dynamics, Ph.D. thesis, Karlsruhe Institute of Technology (KIT), 2020. doi:10.5445/IR/1000124150.

[44] M. Wörner, S. Erdogan, Toward improved closure relations for the turbulent kinetic energy equation in bubble-driven flows, Chemie Ingenieur Technik 85 (2013) 1131–1136. doi:10.1002/cite.201200243.

[45] J. Cano-Lozano, R. Bolanos-Jimenez, C. Gutierrez-Montes, C. Martínez-Bazan, The use of volume of fluid technique to analyze multiphase flows: Specific case of bubble rising in still liquids, Applied Mathematical Modelling 39 (2015) 3290–3305. doi:10.1016/j.apm.2014.11.034.

[46] I. Kataoka, A. Serizawa, Basic equations of turbulence in gas-liquid two-phase flow, International Journal of Multiphase Flow 15 (1989) 843–855. doi:10.1016/0301-9322(89)90045-1.

[47] D. Zhang, N. Deen, J. Kuipers, Numerical simulation of the dynamic flow behavior in a bubble column: A study of closures for turbulence and interface forces, Chemical Engineering Science 61 (2006) 7593–7608. doi:10.1016/j.ces.2006.08.053.

[48] M. Ishii, K. Mishima, Two-fluid model and hydrodynamic constitutive relations, Nuclear Engineering and Design 82 (1984) 107–126. doi:10.1016/0029-5493(84)90207-3.

[49] D. Pfleger, S. Becker, Modelling and simulation of the dynamic flow behaviour in a bubble column, Chemical Engineering Science 56 (2001) 1737–1747. doi:10.1016/S0009-2509(00)00403-6.

[50] E. Olmos, C. Gentric, N. Midoux, Numerical description of flow regime transitions in bubble column reactors by a multiple gas phase model, Chemical Engineering Science 58 (2003) 2113 – 2121. doi:10.1016/S0009-2509(03)00013-7.

[51] R. T. Lahey, The simulation of multidimensional multiphase flows, Nuclear Engineering and Design 235 (2005) 1043 – 1060. doi:10.1016/j.nucengdes.2005.02.020.

[52] A. Tomiyama, I. Kataoka, I. Zun, T. Sakaguchi, Drag coefficients of single bubbles under normal and micro gravity conditions, JSME International Journal Series B 41 (1998) 472–479. doi:10.1299/jsmeb.41.472.

[53] R. Soccol Junior, A. C. Galliani Piscke, D. Noriler, I. C. Georg, H. F. Meier, Numerical analysis of the interphase forces in bubble columns using Euler-Euler modelling framework, The Canadian Journal of Chemical Engineering 93 (2015) 2055–2069. doi:10.1002/cjce.22295.

[54] B. Magolan, N. Lubchenko, E. Baglietto, A quantitative and generalized assessment of bubble-induced turbulence models for gasliquid systems, Chemical Engineering Science: X 2 (2019) 100009. doi:10.1016/j.cesx.2019.100009.

[55] R. Rzehak, E. Krepper, T. Ziegenhein, D. Lucas, A baseline model for monodisperse bubble flows, in: Proceedings of the 10th International Conference on CFD in Oil & Gas, Metallurgical and Process Industries, 2014, pp. 83–91.

[56] D. Legendre, J. Magnaudet, The lift force on a spherical bubble in a viscous linear shear flow, Journal of Fluid Mechanics 368 (1998) 81–126. doi:10.1017/S0022112098001621.

[57] R. Lahey, M. Lopez de Bertodano, O. Jones, Phase distribution in complex geometry conduits, Nuclear Engineering and Design 141 (1993) 177–201. doi:10.1016/0029-5493(93)90101-E.

[58] H. Marschall, R. Mornhinweg, A. Kossmann, S. Oberhauser, K. Langbein, O. Hinrichsen, Numerical simulation of dispersed gas/liquid flows in bubble columns at high phase fractions using OpenFOAM. Part I – Modeling basics, Chemical Engineering & Technology 34 (2011) 1311–1320. doi:10.1002/ceat.201100161.

[59] H. Rusche, Computational fluid dynamics of dispersed two-phase flows at high phase fractions, Ph.D. thesis, Imperial College, London, 2002.

[60] A. Behzadi, R. Issa, H. Rusche, Modelling of dispersed bubble and droplet flow at high phase fractions, Chemical Engineering Science 59 (2004) 759–770. doi:10.1016/j.ces.2003.11.018.

[61] B. Launder, D. Spalding, The numerical computation of turbulent flows, Computer Methods in Applied Mechanics and Engineering 3 (1974) 269–289. doi:10.1016/0045-7825(74)90029-2.

[62] A. Tomiyama, H. Tamai, I. Zun, S. Hosokawa, Transverse migration of single bubbles in simple shear flows, Chemical Engineering Science 57 (2002) 1849–1858. doi:10.1016/S0009-2509(02)00085-4.

[63] A. Bieberle, H.-U. Härting, S. Rabha, M. Schubert, U. Hampel, Gamma-ray computed tomography for imaging of multiphase flows, Chemie Ingenieur Technik 85 (2013) 1002–1011. doi:10.1002/cite.201200250.

[64] L. Schlusemann, G. Zheng, M. Grünewald, Messung der Phasen-verteilung in Blasensäulen, Chemie Ingenieur Technik 85 (2013) 997–1001. doi:10.1002/cite.201300042.

[65] P. Zehner, Mehrphasenströmungen in Gas-Flüssigkeits-Reaktoren, in: E. Blaß, A. Mersmann (Eds.), Reaktionstechnik und Stoffaustauschtech-nik in dispersen Zweiphasensystemen, DECHEMA Monogr. 114, VCH Verlagsgesellschaft, Weinheim, 1989, pp. 215–232.

[66] A. Mersmann, Auslegung und Maßstabsvergrößerung von Blasen- und Tropfensäulen, Chemie Ingenieur Technik 49 (1977) 679–691. doi:10.1002/cite.330490902.